Appl Phys B (2011) 104:331–341
DOI 10.1007/s00340-011-4470-y

Applied Physics B
Lasers and Optics

Influence of soot particle aggregation on time-resolved laser-induced incandescence signals

H. Bladh · J. Johnsson · J. Rissler · H. Abdulhamid · N.-E. Olofsson · M. Sanati · J. Pagels · P.-E. Bengtsson

Received: 19 October 2010 / Revised version: 18 February 2011 / Published online: 13 April 2011

Abstract Laser-induced incandescence (LII) is a versatile technique for quantitative soot measurements in flames and exhausts. When used for particle sizing, the time-resolved signals are analysed as these will show a decay rate dependent on the soot particle size. Such an analysis has traditionally been based on the assumption of isolated primary particles. However, soot particles in flames and exhausts are usually aggregated, which implies loss of surface area, less heat conduction and hence errors in estimated particle sizes. In this work we present an experimental investigation aiming to quantify this effect. A soot generator, based on a propane diffusion flame, was used to produce a stable soot stream and the soot was characterised by transmission electron microscopy (TEM), a scanning mobility particle sizer (SMPS) and an aerosol particle mass analyzer coupled in series after a differential mobility analyzer (DMA-APM). Despite nearly identical primary particle size distributions for three selected operating conditions, LII measurements resulted in signal decays with significant differences in decay rate. However, the three cases were found to have quite different levels of aggregation as shown both in TEM images and mobility size distributions, and the results agree qualitatively with the expected effect of diminished heat conduction from aggregated particles resulting in longer LII signal decays. In an attempt to explain the differences quantitatively, the LII signal dependence on aggregation was modelled using a heat and mass transfer model for LII given the primary particle and aggregate size distribution data as input. Quantitative agreement was not reached and reasons for this discrepancy are discussed.

H. Bladh (✉) · J. Johnsson · N.-E. Olofsson · P.-E. Bengtsson
Division of Combustion Physics, Lund University, P.O. Box 118, 221 00 Lund, Sweden
e-mail: henrik.bladh@forbrf.lth.se
Fax: +46-46-2224542

J. Rissler · H. Abdulhamid · M. Sanati · J. Pagels
Division of Ergonomics and Aerosol Technology, Lund University, P.O. Box 118, 221 00 Lund, Sweden

1 Introduction

Laser-induced incandescence (LII) is an optical diagnostic technique which provides in situ measurements of soot volume fraction and particle size with high temporal and spatial resolution [1, 2]. It has mainly been utilised for measurements in flames (see for example [3–7]), but increasing interest is directed towards applications in cold soot and non-soot particles [8–10]. Although most work has been made in flames and small to moderate-scale combustion systems such as internal combustion engines, the possibility to measure remotely without the use of measurement probes has made the technique interesting also for measurements in large-scale combustion devices, such as aero-engines [11, 12]. LII is based on detection of the increased thermal radiation emitted from soot particles during and after being heated rapidly by a nano-second laser pulse. The peak signal is approximately proportional to the soot volume fraction [13, 14] whereas the decay of the time-resolved signal after the end of the laser pulse will be dependent on the soot particle size. This dependence has its origin in the fact that the main energy loss term in this time region is heat conduction between the hot surface of the particles and the surrounding gas—a mechanism which is dependent on the surface area of the particle as opposed to the internal energy content which is dependent on the particle volume. Hence particles of different size will show varying signal decay times.

Although having been around for some time (the earliest reference to the technique is attributed to Weeks and

Duley in 1974 [15]), there are still issues with regards to signal interpretation and much effort has been directed towards increasing the understanding of the physiochemical mechanisms involved in the laser light interaction with the particles [13, 16, 17]. One important aspect in this context is the influence of soot particle aggregation on the signal. In the early work on soot particle sizing using LII [18, 19] this was not taken into account and the interpreted particle size was basically referred to as the primary particle size—without explicitly accounting for aggregation effects. The first study dealing with this issue was Filippov et al. [20], who presented a model for the influence of particle aggregation on the cooling process. Later, Liu et al. [21, 22] presented improved models taking into account the influence of incomplete thermal accommodation on the shielding effect due to aggregation in the free molecular and transition regimes. Basically, these models predict to what extent the heat conduction per primary particle decreases as function of the level of aggregation. An increased amount of aggregation results in reduced heat conduction for each primary particle in the aggregate compared to a case where the same particles are isolated. This has its origin in the fact that the aggregate structure effectively prevents some parts of the aggregate surface area to be directly accessed by impinging molecules. The models developed for predicting this effect are based on the assumption of fractal-like aggregates. The theoretical calculations by Liu et al. [21] predict a relative decrease of the heat conduction per primary particle of up to 40% for large aggregates when compared to the heat conduction from isolated (non-aggregated) particles of the same sizes. Without taking the shielding effect into account during LII signal evaluation the inferred primary particle size may be overpredicted by as much as a factor of two. In spite of the quite high influence of aggregation predicted by theory, so far little or no experimental evidence has been presented on this effect.

In this study we present measurements on soot particles from a soot generator from which we have been able to produce soot with similar primary particle sizes but different levels of aggregation. The soot generator is based on a quenched propane/air diffusion flame, for which three stable operating conditions were identified and characterised using several different techniques. Scanning mobility particle sizing (SMPS) was carried out to provide the mobility size distribution. The mass of the individual soot aggregates for each bin of mobility size was determined using an Aerosol Particle Mass analyser (APM) coupled in series after a differential mobility analyzer (DMA). Transmission electron microscopy (TEM) of soot sampled using an electrostatic precipitator (EP) was analysed to obtain primary particle size distributions. These results were combined to yield estimates on the primary particle and aggregate size distributions of the particles. Two-colour time-resolved laser-induced incandescence (2C-LII) was then applied in the same measurement location and the signals were analysed to investigate the influence of particle aggregation on the LII signals.

2 Theory and methodology

2.1 Fractal aggregates

A number of studies (see for instance [23] and references therein) have shown that flame-generated particles can be approximated using a statistical scaling law for the mass-fractal structure. This law can be written in terms of the number of primary particles per aggregate, N_p, according to [20, 21]

$$N_p = k_f \left(\frac{R_g}{d_p/2} \right)^{D_f}, \tag{1}$$

where k_f is the fractal prefactor, D_f the fractal dimension, d_p the primary particle size and R_g the radius of gyration of the soot aggregate defined according to

$$R_g^2 = \frac{1}{N_p} \sum_{i=1}^{N_p} (\mathbf{r}_i - \mathbf{r}_0)^2, \qquad \mathbf{r}_0 = \frac{1}{N_p} \sum_{i=1}^{N_p} \mathbf{r}_i, \tag{2}$$

in which the vector $\mathbf{r}_i$ defines the centre of the ith sphere (primary soot particle) within the aggregate and $\mathbf{r}_0$ the aggregate centre [20, 21]. This scaling law has been found to describe the morphology of particles for many types of fuels [23] and is the base assumption used in this work.

2.2 Laser-induced incandescence

The model for laser-induced incandescence (LII) consists of a heat and mass balance equation with which the energy and mass rates are calculated for modelled soot aggregates when they are being exposed to pulsed laser radiation. The model is described in detail elsewhere [13] and only a brief description is given here. As measurements in this work are carried out at low laser fluence, the energy loss due to sublimation of soot matter is assumed to be negligible and the mass conservation equation can be omitted. The energy-balance equation, neglecting the relatively small (∼1%) contribution from radiation losses [24], can be written as

$$\underbrace{\frac{\pi^2 d_p^3 E(m) F}{\lambda} g(t)}_{\text{Absorption}} - \underbrace{\frac{1}{8} \alpha_T \pi D_{\mathrm{HC}}^2 p \sqrt{\frac{8 k_B T_g}{\pi m_g}} \frac{\gamma + 1}{\gamma - 1} \left(\frac{T_p}{T_g} - 1 \right)}_{\text{Heat conduction}} = \underbrace{\frac{\pi}{6} d_p^3 \rho_s c_s \frac{dT_p}{dt}}_{\text{Internal energy}}, \tag{3}$$

where d_p is the primary particle diameter, D_{HC} the effective heat conduction diameter (see later in this chapter), F the laser fluence, $g(t)$ the temporal distribution of laser energy, λ the laser wavelength, α_T the thermal accommodation coefficient, p the gas pressure, k_B the Boltzmann constant, m_g the average molecular weight of the gas molecules, γ the heat capacity ratio of the gas, T_p and T_g the soot particle and gas temperatures, and ρ_s and c_s the density and specific heat of soot, respectively. The heat conduction is the dominant mechanism in the time region starting after the laser pulse and therefore determines the decay time of the signal—large particles have longer decays than small ones. In (3) the heat conduction model has been given explicitly for the free molecular regime to make it possible to see approximately how this sub-mechanism depends on various parameters. All modelled LII signals presented in this work have been derived using the more advanced Fuchs heat conduction model [25]. However, the Fuchs model is more complex and cannot be given analytically in closed form.

For isolated spherical particles in the Rayleigh limit, it becomes relatively straightforward to solve (3). The heat conduction diameter, D_{HC}, will be equal to the primary particle size, d_p. Challenges arise when particles are aggregated and the surface area available for heat conduction decreases. The theoretical model used in this work has been described by Liu et al. [21] and is based on the assumption of fractal-like aggregates following the scaling law given in (1). In this model, an equivalent sphere with diameter D_{HC} is defined as having the same effective area for heat conduction as that of the aggregate. This has been derived by Liu et al. for the free molecular regime using numerical simulations of soot aggregates by direct simulation Monte Carlo (DSMC) with the characteristics described by (1) using $k_f = 2.3$ and $D_f = 1.78$ [21]. The effective heat conduction diameter D_{HC} can be defined as [21]

$$\begin{cases} D_{\mathrm{HC}} = d_p, & N_p = 1, \\ D_{\mathrm{HC}} = (\frac{N_p}{k_h})^{1/D_h} d_p, & N_p > 1, \end{cases} \tag{4}$$

where the scaling parameters k_h and D_h can be written as

$$\begin{cases} k_{h,\mathrm{FM}} = 1.04476 + 0.22329\alpha_T \\ \qquad\qquad + 7.14286 \times 10^{-3}\alpha_T^2, \\ D_{h,\mathrm{FM}} = 1.99345 + 0.30224\alpha_T - 0.11276\alpha_T^2, \end{cases} \tag{5}$$

in which α_T is the thermal accommodation coefficient determining the probability of a molecule to undergo energy exchange with a soot particle during a collision [26]. In this work α_T was set to 0.37 [6] and was not changed or fitted to experimental data as the purpose of the work is to investigate relative differences between signal decay times.

After solving the energy-balance equation for the variables T_p and d_p, the LII signal can be determined using the Planck radiation law combined with the emissivity for soot according to

$$S_{\mathrm{LII}} \propto \pi d_p^2 \frac{4\pi d_p E(m)}{\lambda_{\mathrm{det}}} \frac{2\pi hc^2}{\lambda_{\mathrm{det}}^5} \times \left(\frac{1}{e^{hc/\lambda_{\mathrm{det}} k_B T} - 1} - \frac{1}{e^{hc/\lambda_{\mathrm{det}} k_B T_g} - 1} \right), \tag{6}$$

where h is the Planck constant, and c the speed of light. The detection wavelength, λ_{det}, in (6) is assumed to be single, which is an assumption that can be made if the LII signal is measured using a spectrally narrow-band filter [27]. The model is capable of calculating the LII signal response for both primary particle and aggregate size distributions. The approach follows that of Liu et al. [21] and relies on a set of assumptions, the most important being (1) no influence of nonuniform cooling of the aggregate and (2) the primary particle size may vary between aggregates but is constant in each individual aggregate.

Measurements were made using our two-colour LII (2C-LII) system [27] which enables simultaneous detection of the incandescence at two wavelengths making it possible to infer the soot particle temperature during the LII process using two-colour pyrometry. Particle size evaluation from the two-colour LII data is carried out following the approach described in detail in our previous work [27]. Briefly, it involves calculating the maximum particle temperature using two LII signals and then iteratively run the model for LII while varying the strength of the absorption term, $\dot{Q}_{\mathrm{abs}}$, until model predictions reach the same maximum temperature. LII signals are then modelled and an iterative approach is used to find the least-square fit for a certain parameter (such as d_p, N_p) to the experimental signal curve.

2.3 Equivalent electrical mobility diameter as a measure of aggregate size

The SMPS system has three main components; a bipolar charger, a differential mobility analyzer (DMA), and a condensation particle counter (CPC). The size classification is made by the DMA [28] selecting particles of a given electrical mobility, which is then converted to an equivalent electrical mobility diameter, d_{me}, defined as the diameter of a sphere with the same electrical mobility as the selected particle [29]. In the DMA the electrical force from a variable voltage supply is acting on the particle, the opposing force being the drag force from the surrounding gas. From the velocity caused by the electrical force, d_{me} can be determined. The electrical mobility diameter is independent of the inherent material density of the particle and d_{me} increases for an aggregated soot particle relative to a sphere with the same mass. Note that the latter is opposite to the equivalent heat conduction diameter which is reduced for an aggregated particle compared to a sphere with the same mass. The SMPS

system was used to determine the mobility number size distribution of the aggregates, $N_{agg}(d_{me})$.

2.4 Determining aggregate size distributions from DMA-APM

The number distribution of the aggregates as a function of the number of primary particles contained in each aggregate, $N_{agg}(N_p)$, was used as input for the LII model. This quantity was derived, as described in this section, using the combined knowledge from SMPS ($N_{agg}(d_{me})$), TEM ($N_p(d_p)$) and DMA-APM ($m_{agg}(d_{me})$).

The DMA-APM system is an on-line measurement technique measuring the mass of individual soot aggregates, m_{agg}, of a selected mobility diameter, d_{me} [30]. In the DMA-APM system the DMA selects particles of a given mobility diameter. The quasi monodisperse aerosol is then introduced to the APM by which the mass distribution of the individual aggregates is determined (accounting for the bipolar particle charge distribution). The APM consists of two concentric metal cylinders rotating at the same angular speed. A voltage is applied over the cylinders and only particles of a specific mass-to-charge ratio, for which the centrifugal force is equal to the electrical force, pass the cylinders and are counted by a CPC. The DMA-APM system has been used in a few previous studies, for example [29, 31].

The size distribution of the primary particles, $N_p(d_p)$, was derived from TEM analysis (see Fig. 3). Assuming that the inherent material density of the primary particles is equal to 1.8 g/cm^3 [32], the average mass distributions of the primary particles, $m_p(d_p)$, were calculated. Doing so, the broadening of the primary particle size distribution was taken into account, leading to a slight shift towards larger mean particle diameters for the mass weighted size distribution compared to that of the number weighted size distribution of the primary particles. Using the mass mean of the primary particles, the number of primary particles in the aggregates of a specific mobility diameter was estimated by

$$N_p(d_{me}) = m_{agg}(d_{me})/m_p, \tag{7}$$

where m_p is the mass mean of the primary particle mass size distribution and $m_{agg}(d_{me})$ is known from the DMA-APM measurements. Combining the number size distribution, $N_{agg}(d_{me})$, measured by the SMPS with $N_p(d_{me})$, the number distribution of the aggregates as a function of the number of primary particles contained in one aggregate, $N_{agg}(N_p)$, is obtained.

Previous studies have shown that for soot aggregates formed in diffusion-limited processes, the aggregate mass (and thereby the effective density) as a function of d_{me} is well described by a power law function [33] (compare to the statement made in Sect. 2.1). The exponent has in previous studies been referred to as the mass-fractal dimension of the particles, or the mass mobility scaling factor, d_{fm}. This is similar to the definition of D_f previously introduced (Sect. 2.1) and reveals information about the structure of the soot aggregates. However, since the radius of gyration has not been proven to be linearly proportional to d_{me} over all size ranges, the mass equivalent fractal dimension is not necessarily equivalent to D_f. For this reason we chose to not attempt extracting quantitative data on the morphology from the DMA-APM results in this work. We can, however, compare the d_{fm} derived for the three settings of the soot generator to gain information on relative differences in D_f.

3 Experimental

3.1 The soot generator

The soot under investigation in this work was generated using a soot generator, built in-house, based on the principle of quenching a diffusion flame with a cold gas stream at a specific height—the same principle applied in the commercial CAST system [34]. A more detailed description of the burner is given in another publication [33]. The generator consists of a co-annular burner with propane in the inner tube and air in the outer creating a stable laminar diffusion flame. At 5.5 cm above the burner a horizontal gas stream is introduced with the aim of cooling the flame hence quenching soot formation and oxidation processes. A secondary dilution stage is added in order to achieve a concentration level appropriate for the SMPS and DMA-APM systems. The burner arrangement is shown in Fig. 1. Three stable operating conditions were identified by changing the mass flow rates for propane and air. The quench gas was air and the flow was held constant for all tested cases. The values are given in Table 1 together with the geometric mean diameter determined by SMPS. The variability in GMD and total number concentration was typically on the order of 2 and 5%, respectively (1 std dev.), over the relevant time scale of the experiments [32].

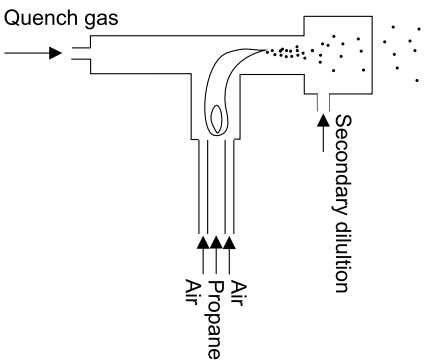

Fig. 1 The soot generator

3.2 Measurement techniques

In order to facilitate both optical and probe diagnostics on the soot from the generator, an open air approach was used (see Fig. 2). The soot generator was positioned at an angle of 45 degrees with respect to the laser beam and detection system, making it possible to switch between LII measurements and probe measurements just by turning off the laser and inserting the measurement probe at the measurement location. The probe techniques are vulnerable to high levels of soot concentration, resulting in potential clogging and coincident detection in the condensation particle counters. LII, on the other hand, relies on the total emitted signal, which means that, as long as the soot cloud is optically thin, it is preferable with a high-level soot concentration. A compromise had to be made, where the level of dilution in the exhaust nozzle of the soot generator (see Fig. 1) and the level of dilution in the sampling head (see Fig. 2) was adjusted so as to maximise the soot volume fraction in the generator exhaust while maintaining accurate readings from the aerosol measurement techniques.

Due to the heavy dilution of the gas stream and hence low concentrations of soot, the 2C-LII setup was designed for optimised sensitivity. It was established that not much could be gained by improving transmission through optical components and sensitivity of the detectors, and, keeping the laser pulse energy just below the level where the heating would cause unwanted sublimation of the soot particles [27], the only alternative was to increase the size of the measurement volume. The 1064 nm laser beam from a Quantel Brilliant B was aligned through an attenuator (Newport model 935-10) and then expanded using a 1:2 telescope resulting in a cross section diameter of ~18 mm ($1/e^2$) enabling a quite large measurement volume. Creating such a large volume required high laser pulse energy. It was therefore not considered possible to create a uniform spatial profile of the laser beam using only the centre portion of the beam and relay imaging [2], as this would waste large parts of the available pulse energy, resulting in a much smaller measurement volume for the same mean fluence. The nonuniform profile of the laser was, however, not considered to be a large source of uncertainty as previously shown by our group [27]. The LII signal was detected using a detection system described in detail elsewhere [27]. It is based on the principle of collecting the spectrally broadband signal using one collection lens ($f = 200$ mm), imaging the signal through an aperture which can be used to determine the spatial resolution along the laser beam, after which the signal is divided into two separate paths. A large aperture (~15 mm diameter) was used to achieve higher sensitivity. The two paths were separately

Table 1 Flow rates of fuel and sheath air and geometric mean diameter (GMD) of particles produced

Case	Fuel/air flow rates (l/min)/(l/min)	Soot particles generated GMD (nm)
A	0.085/3.2	56
B	0.085/3.1	84
C	0.085/3.0	109

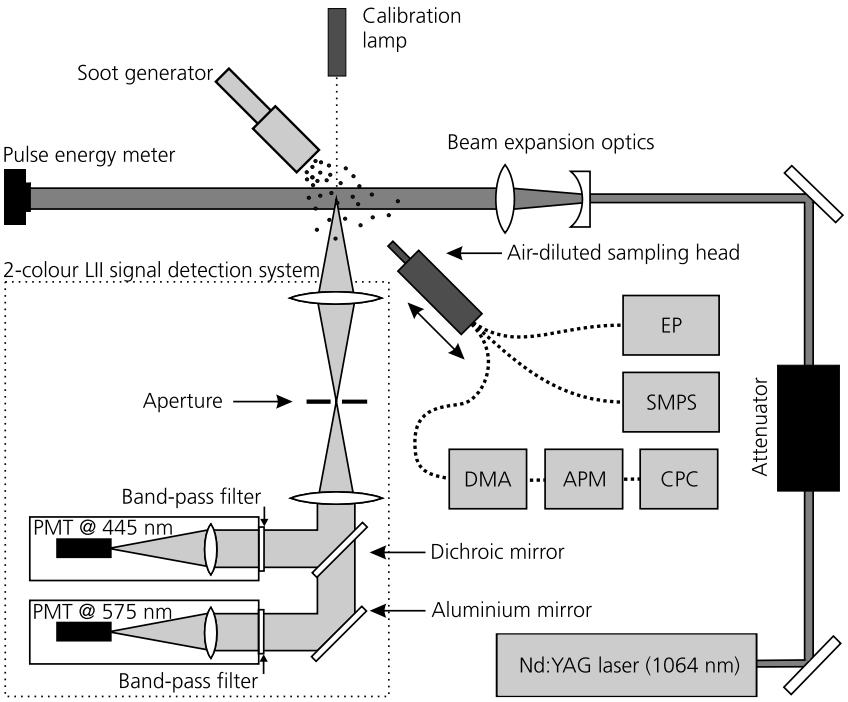

Fig. 2 Schematic of the experimental setup. EP: Electrostatic precipitator, SMPS: Scanning mobility particle sizer, DMA: Differential mobility analyzer, APM: Aerosol particle mass analyzer, CPC: Condensation particle counter

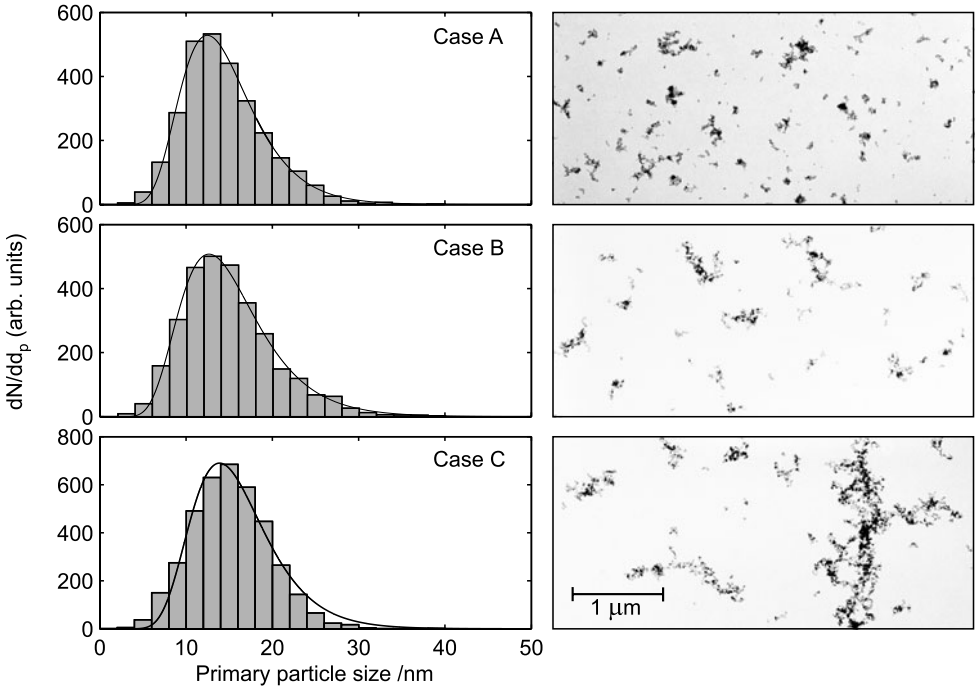

Fig. 3 Primary particle size distributions obtained from TEM analysis together with samples from the images showing increasing level of aggregation from Case A to C. The *solid lines* show the lognormal distribution functions fitted to the data

aligned through spectrally narrow-band filters centred at 445 and 575 nm, respectively, and later imaged onto photomultiplier tubes (PMTs).

To ensure that the laser fluence was low enough to not induce sublimation and thereby potentially influencing the LII signal decay rate, measurements were carried out at three different laser fluences for each case. Peak signals were found to be strongly increasing with laser fluence, while the normalised signals measured for a specific case were almost perfectly overlapping. This ensured that measurements were carried out in the low-fluence regime for all three laser fluences and that the influence of a variation in effective maximum particle temperature on the decay rate was small within the tested fluence range. Surprisingly, maximum particle temperatures evaluated using 2C-LII did not show positive correlation with fluence for all tested cases. We speculate that the problems with the temperature evaluation can be due to the low signal levels from the highly diluted gas stream making the readings sensitive to noise.

Lacking experimentally reliable temperature data, signal evaluation and LII modelling presented in the results section had to be based on an assumed maximum temperature. Model results shown in this work has been based on the assumption of a maximum effective temperature of 3600 K for Case A, but other maximum temperatures within the range covered by the experimentally inferred temperatures were also tested. The difference in signal decay rate was found to be small. The laser fluence and $E(m)$ were held constant in comparisons between the cases.

An ejector diluter (Dekati, Finland) was used to dilute the particle concentration by a factor of ten before the SMPS, DMA-APM and TEM collection. The soot number size distribution based on equivalent electrical mobility diameter was measured just before and after LII measurements using an SMPS system (TSI Inc. model 3934), incorporating a regular DMA operated at a sheath flow rate of 6 lpm and aerosol flow rate of 0.8 lpm. Downstream the DMA a condensation particle counter (CPC, TSI Inc. model 3010) was located. This allowed a measurement range of 10–450 nm with a time-resolution of 180 s. The instrument was calibrated prior to the experiment by using polystyrene calibration nanospheres of known sizes. The number size distribution was inverted to compensate for particle charging, the DMA transfer function, coincidences and losses in the system. DMA-APM measurements were performed the days before and after the LII measurements on all tested cases and analysis of both the DMA-APM and the SMPS data show good repeatability which is seen as evidence that the soot generator provides a stable source for comparative measurements.

Soot was sampled and imaged using transmission electron microscopy (TEM). The soot particles were sampled using the same sample probe that was used for the SMPS measurements and the particles were collected onto thin 3 mm diameter carbon-coated copper grids using an electrostatic precipitator (Nanometer Aerosol Sampler, model 3089 TSI Inc. St Paul, MN, USA). Several grids per test case were used and a total of ∼10 images per case were recorded using a Philips CM-10 electron microscope. The primary particle size was measured manually using the software ImageJ [35]. More than 2800 individual measurements were made for each case.

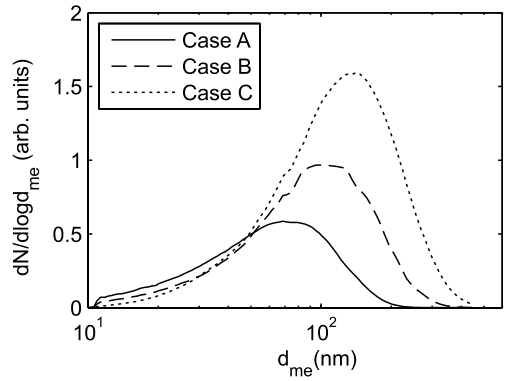

Fig. 4 SMPS number size distribution data

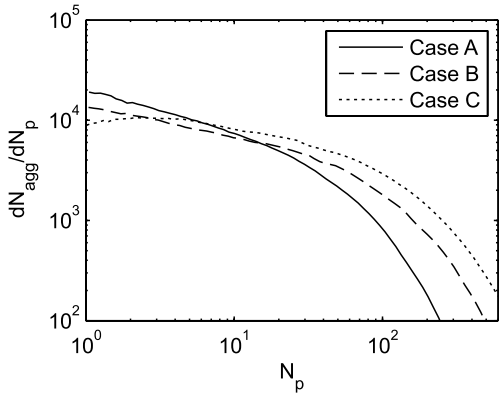

Fig. 5 Aggregate size distributions as a function of N_p in each aggregate obtained by combining SMPS, TEM and DMA-APM data

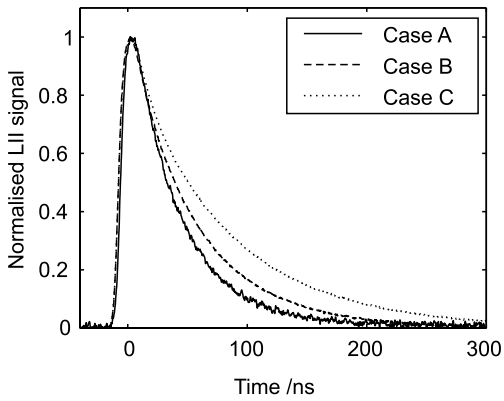

Fig. 6 Shot-averaged experimental LII signals for detection using the 575 nm band-pass filter

4 Results and discussion

4.1 Morphology and size parameters from TEM pictures, SMPS and DMA-APM

A quite large statistical material was analysed on primary particle sizes in the TEM images. The results are shown in Fig. 3 in the representation of histograms with 2 nm bins. The figure shows that the primary particle size distributions obtained from the TEM analysis are similar for the three cases, and that they are well represented using a lognormal size distribution function (the fitted distributions are indicated). The distributions show a peak around 13–15 nm and a half width of ∼12 nm. Contrary to the primary particle sizes, a clear difference could be seen in the level of aggregation, visualised here in the three example images in Fig. 3. Quantitative data on aggregation were, however, not extracted from the TEM data due to the statistical material being insufficient. Aggregate size distributions were instead obtained from the aerosol technology measurement techniques SMPS and DMA-APM.

Figure 4 shows the aggregate number size distributions obtained by the SMPS for the three test cases. It is clearly seen that the aggregate size distribution (mobility diameter) changes between the Cases A, B and C. This is an expected result as the mobility equivalent size is determined by the drag force imposed by the particle movement in the electric field. Hence, it is not only dependent on the primary particle size but also on the number of primary particles in the aggregates, and the particle morphology. The geometric mean diameters of the distributions were 56, 84 and 109 nm, respectively.

The DMA-APM system, measuring the mass of the individual aggregates of selected mobility diameters (here 50, 80, 100, 250 and 400 nm), shows that the mass of the aggregates as a function of d_{me} is well described by a power law function, $m = 4.45 \cdot {d_{\mathrm{me}}}^{2.3}$, where mass is given in grams and d_{me} in meters. No significant differences were observed between Case A, B and C, indicating that the fractal dimension and the primary particle size of the generated particles did not vary between cases. The variation in mass of the aggregates (or the effective density) between scans was within 10% for a given mobility size [33], with no trends over the size range for the three cases tested. This further strengthens the results from the TEM analysis that the primary particles were similar in all three cases.

Using the methodology outlined in Sect. 2.3, combining the results from the DMA-APM system, TEM pictures and SMPS data, the aggregate number distributions as a function of number of primary particles in the aggregates were calculated and the results are shown in Fig. 5. The results agree qualitatively well with aggregate size distributions previously reported [36] and show broad distributions with its maximum at the smallest sizes.

4.2 Analysis of laser-induced incandescence measurements

Shot-averaged time-resolved LII signals for the detection system at 575 nm are shown in Fig. 6. The signal decays

are clearly different, with longer decay time for higher case number. As shown in the previous section, the level of aggregation increases with case number and, as the LII signal decay time is expected to increase with increasing level of aggregation, it now becomes of interest to study this using the theoretical model for the LII signal generation. The analysis will be presented in a step-by-step manner in an attempt to make the reader aware of the predicted influence that can be expected from some parameters influencing size. Finally, the full results, where the measured primary particle and aggregate size distributions are used in the model, will be presented and discussed.

For all theoretical modelling presented in this work a gas temperature of 30 degrees Celsius was assumed for all three cases. The temperature was never measured in situ. The heavy dilution makes the gas stream come close to room temperature, and even if small temperature differences between the cases may have been present (10–20 K) such small differences were found to give minor influence on the signal decay from numerical simulations.

As shown in Fig. 6, the experimentally obtained LII signal decay rates differ significantly. A first natural step is to carry out an evaluation of the primary particle sizes assuming no aggregation, to see to what extent the evaluated sizes would differ between the cases. Note that this evaluation is carried out without regards to the knowledge gained in the last section on the soot particle size distributions. The test is made to simulate a real measurement situation: 2C-LII measurements in an unknown soot source with no prior knowledge on the soot properties.

LII signal evaluation was carried out using the two-colour LII data following the methodology given in Sect. 2.2 with the thermal accommodation coefficient set to 0.37 and the maximum temperature for Case A as 3600 K. The monodisperse equivalent sizes obtained from this evaluation are 19, 26 and 36 nm for Cases A, B and C, respectively. The evaluated size differ by almost a factor of 2 between Cases A and C, results which are not at all supported by the TEM data which suggest similar size distributions (see Fig. 3). This suggests that the reason for the discrepancy must be sought for elsewhere, and the fact that the aggregate distributions are different, as shown both in TEM (Fig. 3) and quantitatively in the DMA-APM data (Fig. 5), it is reasonable to assume that it is the change in heat conduction for different aggregate sizes that is responsible for the different shapes of the LII signals.

In the forthcoming results, two-colour signal evaluation was not made. Instead LII signals were modelled for the 575 nm channel using the laser fluence corresponding to what is needed to provide the maximum temperature 3600 K for Case A. This laser fluence was then used for all three cases in a comparison. The modelling was done using a top-hat spatial profile of the laser and a Gaussian temporal profile with the full width at half maximum similar to what was used during the experiment. As the spatial profile of the laser was Gaussian during the experiments, the cases with monodisperse aggregate sizes were modelled for both a top-hat and Gaussian beam profile for comparison. The results were nearly identical. The reason for not providing results based on a Gaussian beam profile is that the current implementation of the LII model is not able to use a nonuniform profile when using aggregate size distribution functions as input. Using this methodology, conclusions are drawn from the appearance of the LII signals only. Note that in order to reach absolute agreement between model and experiment, the thermal accommodation coefficient would have to be fitted to the experimental data. As previously mentioned, this has not been done in this work as the scope is merely to compare the relative appearance between Cases A, B and C.

As was shown in Fig. 3, the measured primary particle size distributions are similar for the three cases. However, as they are not identical, it is of interest to investigate to what extent they affect the LII signal decay rate. For this purpose the LII model was used to create three time-resolved signals, one for each case, using the fitted lognormal size distributions presented in Fig. 3 as input. As aggregation was neglected in this test, the only difference expected on the signal decay rate has its origin in the slightly different primary particle size distributions. The results are shown in Fig. 7a. As can be seen, the estimated influence of the small differences in the primary particle size distributions from Cases A, B, and C is minor.

In a second test, the aggregation model by Liu et al. [21] was turned on to try to replicate the results from the experiments. Figure 7b shows the results obtained when assuming monodisperse aggregate size distributions with values of N_p chosen to be rough estimates of the aggregate sizes seen in the TEM images. Here the results deviate more and actually resemble the deviations seen in the experimental data. Obviously the level of aggregation has potential to explain the difference in the decay rate of the experimentally obtained LII signals, but it must be kept in mind that the monodisperse aggregate sizes chosen in Fig. 7b are quite far from each other in size and will give rise to a quite pronounced difference in predicted relative energy loss through heat conduction. Additionally, they are monodisperse, meaning that they do not take into account the large averaging effect expected from a realistic aggregate size distribution. Figure 7b should therefore only be seen as an example of what is the maximum effect possible to obtain when using the Liu model.

In an attempt to estimate the effect of changed heat conduction on the LII signals from the real aggregate size distributions, the distribution functions obtained from the DMA-APM (Fig. 5) and the lognormal particle size distributions

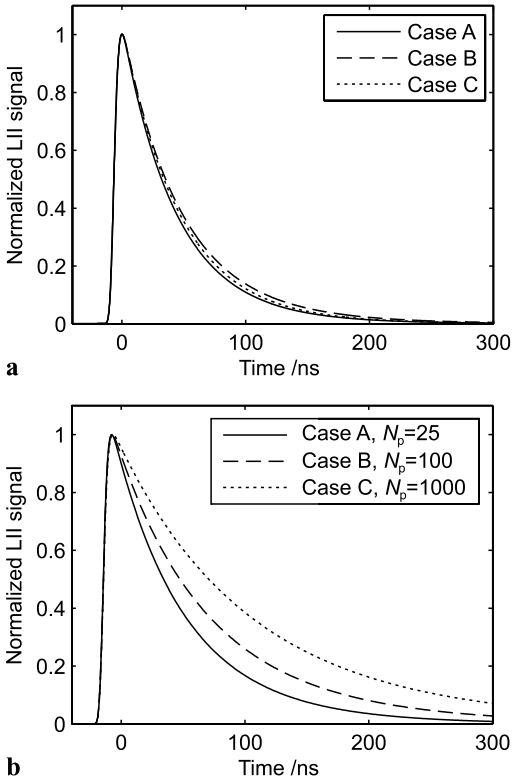

Fig. 7 Normalised modelled LII signals for the three cases. In (**a**) the aggregation submodel was turned off to visualise the influence of the primary particle size distributions obtained from TEM analysis on the results, whereas in (**b**) the submodel was turned on and given three monodisperse aggregate size distributions as input

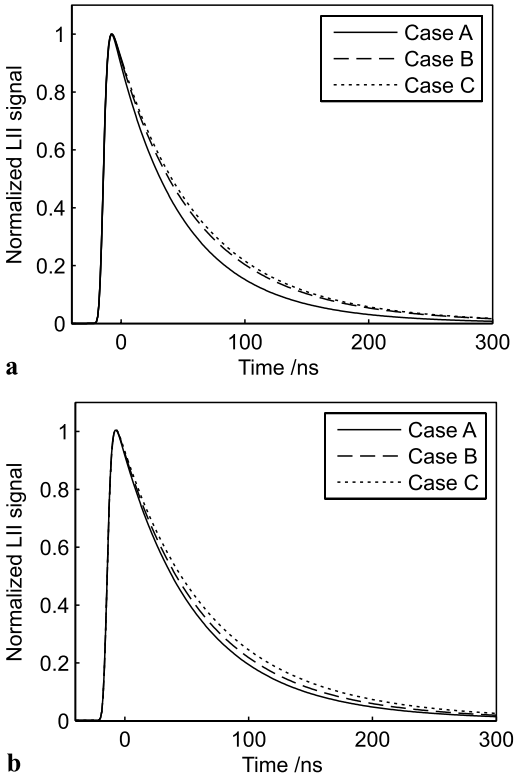

Fig. 8 Modelled LII signals using the experimentally determined primary particle and aggregate size distributions. In (**a**) the results were obtained by using the three lognormal size distributions shown in Fig. 3 together with the aggregate size distributions shown in Fig. 5. In (**b**) a single lognormal distribution fitted to the TEM data of all three series and aggregate size distributions determined using this single distribution was used to create the signals

fitted to the TEM data (Fig. 3) was given as input to the model, the results being shown in Fig. 8a. The results do indeed show contributions from the level of aggregation. Contrary to the results obtained with no aggregation (Fig. 7a) the signal decay times shown in Fig. 8a increases steadily with case number—a behaviour that was also found experimentally. The differences are, however, less pronounced in the theoretical results. While the difference between the signals of Cases A and B seem to follow the experimental results reasonably well, Case C is estimated to appear very close to Case B as opposed to what was found experimentally where the signals from Cases B and C are quite different.

The question is to what extent the primary particle size distributions affect the results. Arguable, the three cases show similar distributions (see Fig. 3), but as these data are used both directly in the LII model and for evaluating the aggregate size distributions which are also used in the LII model, the distributions may affect the signal decays in a not so obvious way. To shed some light on this matter, a single lognormal distribution function was fitted to all three TEM data series and, based on this distribution, a new set of aggregate size distribution functions were determined. These have a quite similar, but not identical, appearance when plotted in the log–log representation used for Fig. 5. The lognormal particle size distribution and these new aggregate size distributions were used as input to the model for LII and time-resolved LII signals were calculated. The results are shown in Fig. 8b. The signal decays now appear more uniformly spaced, quite contrary to what was the case in the results obtained using individually determined primary particle size distributions (Fig. 8a). Obviously, the influence of primary particle size on the modelled results is substantial, and it thus becomes challenging to isolate the influence of aggregation from the influence of the primary particle size distributions in this study.

Some conclusions can be drawn from the analysis. Firstly, it becomes clear that the present LII model is unable to explain the large difference in signal decay rate seen in the experimental results. There are many potential reasons for this. Clearly, each measurement technique and methodology suffers from, and introduces, uncertainty and the true distributions of primary particle and aggregate size may be somewhat different than what was obtained in this work. However, in order for the LII model to replicate what is seen ex-

perimentally, quite large deviations in the input size distributions are needed, and, even if it cannot be completely ruled out, it becomes less plausible as a sole explanation. Also, the Liu model [21] must be regarded as a potential source of uncertainty in this work. Firstly, it has been derived for the free molecular regime. As measurements presented in this study are likely to occur in the transition regime due to the low gas temperature, deviations can be expected. Secondly, the Liu model has been derived using fractal dimensions for flame soot not necessarily applicable for the soot from the generator. Indeed, one may interpret the DMA-APM data as indicating that the fractal exponent is larger than 1.78, which is assumed in the Liu model. Thus it becomes of interest to investigate how theory predicts energy loss through heat conduction as function of mass-fractal dimension. In order to do this, a Monte Carlo approach similar to the one used by Liu et al. will be needed to derive the empirical constants D_h and k_h from the mass-fractal dimensions, but this is beyond the scope of the present work. It will also be necessary to investigate the influence of aggregation on other sub-mechanisms in the LII model, for instance the absorption rate [37].

In an attempt to find explanations for the behaviour of the experimental LII signals seen in Fig. 6, the assumptions made for the soot properties must be scrutinised. It is assumed in this work that the soot optical and physical properties do not differ significantly between the tested cases, but a difference cannot be ruled out. The soot optical properties may vary between the cases as a result from the quenching being carried out at different flame heights, introducing soot in the exhaust stream from different soot regions including both nascent and more mature particles [38]. Additionally, the particles may be exposed to a varying degree of volatiles in the exhaust stream which means that particle coating may be present to a varying degree between the cases due to the different gas compositions. However, measurements performed with a burner using the same principle as the one used here showed very small amounts of organic material (<5%) which did not vary with increasing air-to fuel mass flow rate ratio [33]. Furthermore, a changing degree in coating would result in changing $m_p(d_{\mathrm{me}})$ and this was not observed in the DMA-APM measurements. Also, the thermal accommodation coefficient can introduce a significant uncertainty in the experimental data, as it may vary between the cases resulting from different particle surface structure and/or ambient gas composition. However, these effects are minimised using a high-velocity quench gas followed by a high level of dilution in the exhaust nozzle and are not expected to be a significant source of uncertainty. Additionally, soot examined using TEM and DMA-APM did not show differences in morphology and primary particle shape.

5 Summary and conclusions

In this work we present what is believed to be the first experimental investigation with the aim of quantifying the influence of particle aggregation on the decay rate of laser-induced incandescence (LII) signals. A soot generator producing exhausts with stable properties was developed and three operating conditions were identified that were found to produce particles of similar primary particle sizes but very different levels of aggregation. Two-colour LII was carried out for the three cases resulting in signal decay rates quite different from each other. The soot properties were determined using a battery of diagnostic techniques including transmission electron microscopy (TEM), scanning mobility particle sizer (SMPS) and a differential mobility analyzer coupled in series with an aerosol particle mass analyzer (DMA-APM). From the TEM data the primary particle size distributions were derived. The aggregate size distributions were derived using a combination of the TEM, SMPS and DMA-APM data.

A model for LII was used to analyse the experimentally obtained LII signals. This investigation shows:

1. Neglecting to take aggregation into account results in predicted LII signals with essentially identical decay rates for the three cases, as opposed to the experimental signals which are clearly different.
2. Using the submodel to account for the reduced heat conduction for aggregated particles, it was possible to obtain agreement between experiment and theory, but only for unrealistic aggregate distribution functions.
3. Using the aggregate size distribution functions derived from the experimental data, the model could replicate the observed trends but was not able to explain the large differences in LII signal decay rate for the three cases.

All theoretical investigations in this work are based on a submodel for aggregation derived by Liu et al. [21] for the free molecular regime and, additionally, for flame soot which do not necessarily show morphology similar to the soot investigated in this study. Future work will include development of our own code to determine the shielding effect from aggregates with more appropriately chosen morphology, and, more generally, an improvement of the theoretical model for LII with special focus on the influence of aggregation on the various sub mechanisms.

Acknowledgements The financial support from the J. Gust. Richert Foundation, the Swedish Research Council (VR), and FORMAS are gratefully acknowledged. We thank Dr. Eric Carlemalm at the Department of Electron Microscopy at the Faculty of Medicine at Lund University for the operation of the transmission electron microscope.

References

1. R.J. Santoro, C.R. Shaddix, in *Applied Combustion Diagnostics* (Taylor and Francis, New York, 2002), p. 252
2. C. Schulz, B.F. Kock, M. Hofmann, H. Michelsen, S. Will, B. Bougie, R. Suntz, G. Smallwood, Appl. Phys. B **83**, 333 (2006)
3. P.-E. Bengtsson, M. Aldén, Appl. Phys. B **60**, 51 (1995)
4. S. De Iuliis, F. Cignoli, G. Zizak, Appl. Opt. **44**, 7414 (2005)
5. T. Lehre, B. Jungfleisch, R. Suntz, H. Bockhorn, Appl. Opt. **42**, 2021 (2003)
6. D.R. Snelling, F.S. Liu, G.J. Smallwood, Ö.L. Gülder, Combust. Flame **136**, 180 (2004)
7. S. Will, S. Schraml, K. Bader, A. Leipertz, Appl. Opt. **37**, 5647 (1998)
8. Z.H. Lim, A. Lee, K.Y.Y. Lim, Z. Yanwu, S. Chorng-Haur, J. Appl. Phys. **107**, 064319 (2010), 7 pp.
9. B.F. Kock, C. Kayan, J. Knipping, H.R. Orthner, P. Roth, Proc. Combust. Inst. **30**, 1689 (2005)
10. R. Starke, B. Kock, P. Roth, Shock Waves **12**, 351 (2003)
11. J. Delhay, P. Desgroux, E. Therssen, H. Bladh, P.-E. Bengtsson, H. Hönen, J. Black, I. Vallet, Appl. Phys. B **95**, 825 (2009)
12. J.D. Black, M.P. Johnson, Aerosp. Sci. Technol. **14**, 329 (2010)
13. H. Bladh, J. Johnsson, P.-E. Bengtsson, Appl. Phys. B **90**, 109 (2008)
14. L.A. Melton, Appl. Opt. **23**, 2201 (1984)
15. R.W. Weeks, W.W. Duley, J. Appl. Phys. **45**, 4661 (1974)
16. H.A. Michelsen, J. Chem. Phys. **118**, 7012 (2003)
17. F. Goulay, P.E. Schrader, L. Nemes, M.A. Dansson, H.A. Michelsen, Proc. Combust. Inst. **32**, 963 (2009)
18. S. Will, S. Schraml, A. Leipertz, Opt. Lett. **20**, 2342 (1995)
19. P. Roth, A.V. Filippov, J. Aerosol Sci. **27**, 95 (1996)
20. A.V. Filippov, M. Zurita, D.E. Rosner, J. Colloid Interface Sci. **229**, 261 (2000)
21. F. Liu, M. Yang, F.A. Hill, D.R. Snelling, G.J. Smallwood, Appl. Phys. B **83**, 383 (2006)
22. F. Liu, G.J. Smallwood, in *40th Thermophysics Conference* (Seattle, Washington, 2008)
23. Ü.Ö. Köylü, G.M. Faeth, T.L. Farias, M.G. Carvalho, Combust. Flame **100**, 621 (1995)
24. S.-A. Kuhlmann, J. Reimann, S. Will, J. Aerosol Sci. **37**, 1696 (2006)
25. A.V. Filippov, D.E. Rosner, Int. J. Heat Mass Transf. **43**, 127 (2000)
26. K.J. Daun, G.J. Smallwood, F. Liu, J. Heat Transf. **130**, 121201 (2008), 9 pp.
27. H. Bladh, J. Johnsson, P.-E. Bengtsson, Appl. Phys. B **96**, 645 (2009)
28. E.O. Knutson, K.T. Whitby, J. Aerosol. Sci. **6**, 443 (1975)
29. K. Park, D. Dutcher, M. Emery, J. Pagels, H. Sakurai, J. Scheckman, S. Qian, M.R. Stolzenburg, X. Wang, J. Yang, P.H. McMurry, Aerosol Sci. Technol. **42**, 801 (2008)
30. K. Park, F. Cao, D.B. Kittelson, P.H. McMurry, Environ. Sci. Technol. **37**, 577 (2003)
31. J. Pagels, A.F. Khalizov, P.H. McMurry, R.Y. Zhang, Aerosol Sci. Technol. **43**, 629 (2009)
32. K. Park, D.B. Kittelson, M.R. Zachariah, P.H. McMurry, J. Nanopart. Res. **6**, 267 (2004)
33. A. Malik, H. Abdulhamid, J. Pagels, J. Rissler, M. Lindskog, R. Bjorklund, P. Jozsa, J. Visser, A. Spetz, M. Sanati, Aerosol Sci. Technol. **45**, 1 (2011)
34. CAST, Combustion Aerosol Standard (Jing Ltd., Im Park 4, CH-3052 Zollikofen BE, Switzerland). http://www.sootgenerator.com. Available September 2010
35. W.S. Rasband, *ImageJ* (U.S. National Institutes of Health, Bethesda, MD, USA, 2007). http://rsb.info.nih.gov/ij/. Available September 2010
36. K. Tian, F.S. Liu, K.A. Thomson, D.R. Snelling, G.J. Smallwood, D.S. Wang, Combust. Flame **138**, 195 (2004)
37. F. Liu, G.J. Smallwood, J. Quant. Spectrosc. Radiat. Transf. **111**, 302 (2010)
38. H. Bladh, J. Johnsson, N.E. Olofsson, A. Bohlin, P.E. Bengtsson, Proc. Combust. Inst. **33**, 641 (2011)